Dalton Transactions

ROYAL SOCIETY OF CHEMISTRY

PAPER

View Article Online
View Journal

Cite this: DOI: 10.1039/d5dt01416f

An *in situ* dual modification strategy for enhancing the electrocatalytic oxygen evolution performance of ZIF-67

Rajesha Kumar Swain,† Aranya Kar, † Aditi Halder and Chullikkattil P. Pradeep *

Enhancing the electrocatalytic performance of metal–organic frameworks (MOFs) remains a key challenge in energy materials research. In this study, the cobalt-based zeolitic imidazolate framework ZIF-67 (**Z67**) was modified using an all-inorganic coordination polymer, $\{(H_2O)_2K\text{-}\mu\text{-}(H_2O)_3Ni(H_2O)_3\}_{2n}[V_{10}O_{28}]_n$ (**NiV$_{10}$**), which introduces both nickel (Ni) centers and decavanadate (V_{10}) polyoxometalate (POM) clusters into the framework. An *in situ* synthetic approach was employed to generate a series of nanocomposites (**25NZ67**, **50NZ67**, and **75NZ67**) by varying the amount of **NiV$_{10}$** added during **Z67** synthesis. The integration of Ni^{2+} and V_{10} clusters led to a significant structural reorganization in the **Z67** framework, leading to the formation of a more open architecture, unlocking coordinatively unsaturated metal active sites (CUMAS), and enriching the material with abundant electroactive centres. Electrochemical evaluation revealed significantly improved oxygen evolution reaction (OER) performance for all composites compared to pristine **Z67**. The onset potential for all three composites was in the range of 1.44–1.46 V. The composite **75NZ67** exhibited an overpotential of 350 mV at j = 10 mA cm^{-2}, which was ~200 mV and ~130 mV lower than **Z67** and **NiV$_{10}$**, respectively, at the same current density. Further, **75NZ67** exhibited the highest OER activity, with a 3-fold increase in current density compared to pristine **Z67**. It also displayed an improved Tafel slope of 120 mV dec^{-1}, outperforming most of the control compounds studied and **Z67** (144 mV dec^{-1}). The encapsulation of POM within the ZIF cavity reduces the charge transfer resistance, leading to improved electrochemical performance during OER, as evidenced by the linear sweep voltammetry (LSV) curves. Notably, **25NZ67** demonstrated the best long-term stability, maintaining its performance over extended operation, and also the highest intrinsic activity when normalized by electrochemical surface area (ECSA). Control experiments confirmed that the enhanced activity arises from the synergistic effect of Ni doping and V_{10} encapsulation, achievable only *via* the *in situ* synthetic route. This work highlights a room-temperature *in situ* design strategy for **Z67**-based electrocatalysts by leveraging transition metal–polyoxometalate hybridization for improved OER performance.

Received 16th June 2025,
Accepted 10th August 2025

DOI: 10.1039/d5dt01416f

rsc.li/dalton

Introduction

One of the most critical reactions in electrochemical energy conversion and storage is the oxygen evolution reaction (OER). The high potential (1.23 V) and the slow reaction kinetics of OER brought about by the four-electron and proton transfer process result in low electrolysis efficiency.[1] High-performing materials based on noble metals like Ir and Ru are employed in most well-known electrocatalysts.[2,3] However, their large-scale commercial development is significantly hindered by low reversibility, high cost, and scarce abundance on Earth. It is, therefore, vital to explore inexpensive, highly abundant, and non-toxic catalysts that have the benefits of low overpotential, extended stability, and faster reaction rates. To date, numerous materials have been reported as OER electrocatalysts, including, but not limited to, transition metal oxides,[4] chalcogenides,[5] layered double hydroxides (LDH),[6] coordination polymers (CPs),[7] metal organic frameworks (MOFs)[8] and polyoxometalates (POMs).[9]

ZIF-67 (**Z67**) is one of the most widely studied zeolitic imidazolate frameworks (ZIFs) containing cobalt as the metal center and 2-methylimidazole (2-MeIm) as ligands. It serves as a potential candidate for OER electrocatalyst but suffers from poor intrinsic activity. The Co centres in **Z67** are coordinatively saturated, hindering the adsorption of water molecules.

School of Chemical Sciences, Indian Institute of Technology Mandi, Mandi, Himachal Pradesh – 175005, India. E-mail: pradeep@iitmandi.ac.in; Fax: +911905267 009; Tel: +91 1905 267 045

† These authors contribute equally to the manuscript.

Various strategies have been adopted to tackle this drawback and fine-tune the electrocatalytic activity of pristine **Z67**.[10,11] These include, synthesizing bi-metallic ZIFs,[12,13] thermal treatment,[14,15] composite formations,[16,17] and encapsulating other catalytically active materials in ZIF cavities.[18–20] Such strategies lead to the formation of coordinatively unsaturated metal active sites (CUMAS) in the ZIF framework, boosting its electrocatalytic activity. In terms of incorporating a second metal, Ni-doped ZIFs have been a popular choice. Introduction of Ni modifies the electronic environment of cobalt centres in **Z67**, improving intrinsic catalytic activity and facilitating the formation of active NiOOH and CoOOH species. Even very low concentrations (0.001 M) of Ni^{2+} have been reported to significantly boost the OER performance of **Z67**.[21] Li and co-workers designed Co–Ni bimetallic metaphosphate nanoparticles ($Co_{1.6}Ni_{0.4}P_4O_{12}$-C) derived from a Co–Ni ZIF, which showed appreciable alkaline OER activity. Their DFT calculations revealed that Ni doping resulted in facile binding of the oxygenated intermediates to the catalyst surface.[22] Liu *et al.* also reported the synthesis of ZIF-67@Ni@FeOOH composite employing a dual approach of doping Ni in **Z67** framework and simultaneous structural defect engineering by FeOOH. The material displayed high electrocatalytic OER activity and also revealed NiOOH and CoOOH formation during the reaction, as the active species.[23]

Notably, another widely used strategy of **Z67** activation is encapsulation of other catalytically active materials such as POMs, which are nanosized metal oxide clusters of early transition metals (Mo, W, V and Nb) present in their highest oxidation state.[24] They are potential precursors for multifunctional materials due to their nanosized architecture, robust nature, highly polarized oxygen-rich surface, and innate catalytic qualities.[25–27] POMs also have significant benefits in electrocatalysis due to their excellent redox properties, ability to act as electron shuttling units, selectivity, and corrosion resistance, which make them useful as adaptable inorganic ligands for OER electrocatalysts.[25,27–29] K. Abdelkader *et al.* successfully synthesized **Z67**@POM hybrids using a tri-cobalt substituted lacunary Keggin POM ($[SiW_9Co_3O_{40}]$). The material exhibited superior OER performance due to the synergistic interaction between POM and **Z67** and the structural distortions of **Z67** in the material.[30] In another notable work, Li and co-workers reported a unique yolk/shell structured **Z67**@POM catalyst with a Keggin ($[PW_{12}O_{40}]^{3-}$) POM. The structural arrangement showed POM nanoparticles coated on **Z67**, and the synergistic effect of the two components resulted in its high activity as an OER electrocatalyst.[17] Recently, vanadium(v) based materials have also gained much interest for applications like rechargeable batteries,[31] supercapacitors,[32] and OER electrocatalysts,[31] due to their excellent electrochemical properties and high earth abundance. Among the different POM variants, vanadium-based POM decavanadate ($H_2[V_{10}O_{28}]^{4-}$), has scarcely been explored for electrocatalysis despite its potential.[32–34] Meanwhile, Wei and co-workers have reported that the doping of pentavalent V in the spinel oxides (Co_3O_4 and $NiFe_2O_4$) can enhance their activity and stability toward electrocatalytic OER application.[35]

The above discussions imply that different strategies can activate a metal–organic framework, such as **Z67**, towards electrocatalytic OER. A combination of such strategies can certainly lead to interesting catalytic materials.[36] In this study, we investigate the activation of **Z67** for electrocatalytic OER by incorporating a nickel-decavanadate-based all-inorganic coordination polymer, $\{(H_2O)_2K\text{-}\mu\text{-}(H_2O)_3Ni(H_2O)_3\}_{2n}[V_{10}O_{28}]_n$ (**NiV_{10}**). Here, **Z67** host was synthesized in a simple room-temperature *in situ* method in the presence of pre-dissolved **NiV_{10}** polymer. This approach was designed to enable both the doping of heterometal (Ni^{2+}) ions into the **Z67** framework and the encapsulation of a POM unit, decavanadate (V_{10}) cluster, within the **Z67** cavities simultaneously. The labile aqua ligands coordinating the Ni centres in **NiV_{10}** are expected to dissociate under synthetic conditions, facilitating Ni incorporation and cluster encapsulation during **Z67** formation. In this way, three composites (**25NZ67**, **50NZ67**, and **75NZ67**) were synthesized by varying the amount of **NiV_{10}** introduced (25/50/75 mg) into the **Z67** synthetic medium (Scheme 1). Structural and spectroscopic analyses confirmed both the doping of Ni^{2+} and the distribution of V_{10} clusters within the cavities and on the surface of the **Z67** framework. These modifications led to the formation of a more open architecture, unlocked coordinatively

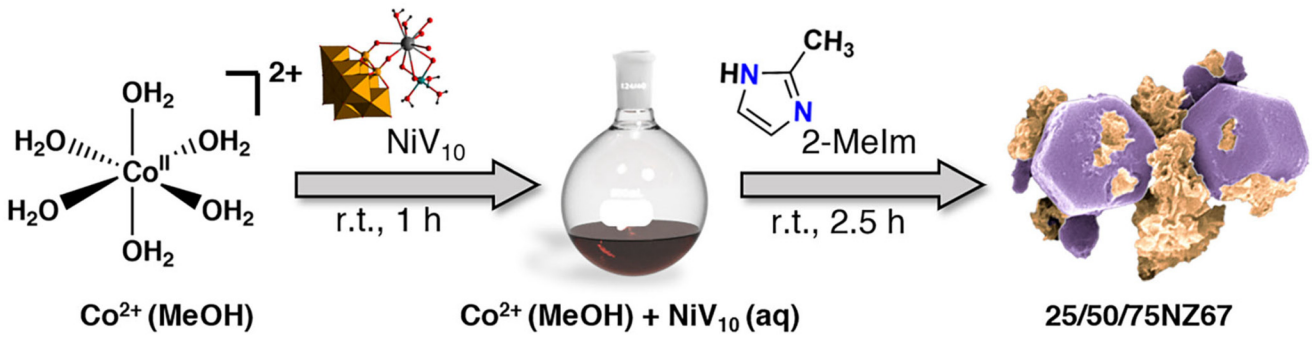

Scheme 1 Synthetic scheme for **25/50/75NZ67** composites. The yellow polyhedra of **NiV_{10}** denotes decavanadate cluster, with Ni (green) and K (gray) centers attached. The composite is shown by selective coloring of FESEM image, where the violet areas denote Ni-doped **Z67**, and the orange-colored regions denote the V_{10}. (**NiV_{10}**: $\{(H_2O)_2K\text{-}\mu\text{-}(H_2O)_3Ni(H_2O)_3\}_{2n}[V_{10}O_{28}]_n$; 2-MeIm: 2-methylimidazole).

unsaturated metal active sites (CUMAS), and enriched the material with abundant Co^{3+} electroactive centers.[18,19] Electrochemical evaluation revealed significantly improved OER performance for all composites compared to pristine **Z67**, with **75NZ67** exhibiting the highest activity, while **25NZ67** demonstrated the best long-term stability. Our strategy reported here is different from some of the previously employed strategies[37–41] to modify ZIFs and its significance is also underscored by the fact that our catalysts (**25/50/75NZ67**) outperformed some of the previously reported **Z67** based OER catalysts (Co-ZIF-9 (510 mV),[37] ZIF-67/NPC-2 (410 mV)[38] and ZIF-8@ZIF-67@POM (490 mV)[16]) in terms of overpotential (η) value at 10 mA cm^{-2} of current density by a margin of *ca.* 40–140 mV. These results highlight the effectiveness of combining metal substitution and POM encapsulation to engineer MOF-based electrocatalysts with enhanced activity and durability for alkaline OER.

Results and discussion

The synthesis of the coordination polymer **NiV_{10}** ($\{(H_2O)_2K\text{-}\mu\text{-}(H_2O)_3Ni(H_2O)_3\}_{2n}[V_{10}O_{28}]_n$) was performed by following a reported procedure.[34] The nanocomposites, **25NZ67**, **50NZ67** and **75NZ67**, were fabricated *in situ* by synthesizing **Z67** host in the presence of different amounts (25, 50 and 75 mg) of pre-dissolved **NiV_{10}** in the reaction medium. The synthesized materials were characterized using different characterization techniques, including attenuated total reflection Fourier transform infrared spectroscopy (ATR-FT-IR), inductively coupled plasma-mass spectrometry (ICP-MS), X-ray diffraction (XRD), N_2-adsorption–desorption, X-ray photoelectron spectroscopy (XPS), thermogravimetric analysis (TGA), transmission electron microscopy (TEM), scanning electron microscopy with energy-dispersive X-ray spectroscopy (SEM/EDS), cyclic voltammetry (CV), and differential pulse voltammetry (DPV). The Experimental section gives technical information regarding these analyses.

Fig. 1a shows the FT-IR spectra of **Z67**, **NiV_{10}**, and all three as-prepared composites. The characteristic peaks of 2-MeIm appeared at 694 cm^{-1} (C–H bending), 752 cm^{-1} (C–H bending), 994 cm^{-1} (=C–H in-plane bend), 1380 cm^{-1} (CH_3 asymmetric bend), 1424 cm^{-1} (CH_2 asymmetric bend) and 1585 cm^{-1} (C=N stretch). Additionally, the peak at 421 cm^{-1} represents the Co–N stretching mode, which confirms the presence of **Z67** in all the composites.[39,40] The FT-IR spectra of the composites also indicated the presence of V_{10} clusters, as evident from the peaks at 983 and 840 cm^{-1}, ascribed to the terminal V=O bond stretches, and weaker peaks at 809 and 530 cm^{-1} corresponding to the symmetric V–O–V vibrations.[34] In all the composites, a peak broadening was noticed between 550 and 950 cm^{-1}, indicating the interaction between **Z67** and the V_{10} clusters of **NiV_{10}**.[41] This peak broadening increases from **25NZ67** to **75NZ67**, pointing to the increased V_{10} content in the composites.

The XRD pattern of the as-synthesized **Z67** (Fig. 1b) exhibited the characteristic peaks at 7.4°, 10.5°, 12.6°, and 17.8°, corresponding to the (011), (002), (112), and (222) diffraction planes, respectively, confirming the formation of pure phase **Z67** (Fig. S1).[40,42] The XRD patterns of the composites closely resembled that of **Z67**, indicating that the **Z67** crystal structure remains largely intact during composite formation, as expected. **NiV_{10}**, due to its labile linkage between Ni and decavanadate centers, forms decavanadate clusters and Ni^{2+} hydrated species in solution. Given that the decavanadate POM has a size of approximately 0.8–1 nm, it can fit within the 1.16 nm cages of **Z67**, resulting in its effective encapsulation and preventing the formation of any separate crystalline phase in the composite (especially for lower loading samples like **25NZ67**). Additionally, the POM becomes highly dispersed in these composites at a molecular or sub-nanometer scale, which prevents it from exhibiting distinct crystalline peaks in the PXRD pattern. Similar observations have been reported where POM incorporation does not alter the host framework diffraction due to the absence of long-range ordered POM domains.[16,19] The average crystallite size of **Z67**, determined using the Scherrer equation, was 50.11 nm, which decreased to 40 nm in **25NZ67**.[18,19] In **50NZ67** and **75NZ67**, the crystallite sizes were 39 nm and 38 nm, respectively. This decrease in the crystallite size indicates that the interaction between the V_{10} and **Z67** seems to interfere with the growth of **Z67** crystals, making them smaller, as reported earlier.[18,19] Along with that, the overall crystallinity of the samples also showed a decrease when moved from **Z67** to **75NZ67**, as evident from the decreased intensity of the PXRD peaks.

To evaluate the surface area and pore sizes of the **25/50/75NZ67** composites, we analysed their N_2 adsorption–desorption isotherms, see Fig. 2. The results revealed a consistent decrement in the BET surface area of all composites compared to **Z67** (1102.99 m^2 g^{-1}). Further, it can be noted that the surface area consistently decreases with increasing feed ratio of **NiV_{10}** loading in the composites, from 764.97 m^2 g^{-1} for **25NZ67** to 483.54 m^2 g^{-1} for **50NZ67** and 356.10 m^2 g^{-1} for **75NZ67**. These observations are also consistent with the previous reports.[17,18] The incorporation of V_{10} clusters into the pores and the surface of **Z67** particles is responsible for this decrease in surface area. Along with the decrement in BET surface area, a gradual decrease in the pore volume of the

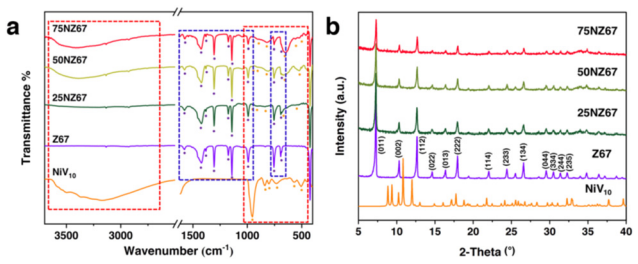

Fig. 1 (a) FT-IR spectra of **NiV_{10}**, **Z67** and **25/50/75NZ67** (orange dots indicated the peaks originating from the **NiV_{10}** incorporation, violet dots are the peaks responsible for **Z67** framework. Red dotted boxes indicate the area where decavanadate peaks can be observed, and the violet dotted boxes denote the area where **Z67** peaks can be observed.); (b) XRD spectra of **NiV_{10}**, **Z67** and **25/50/75NZ67**.

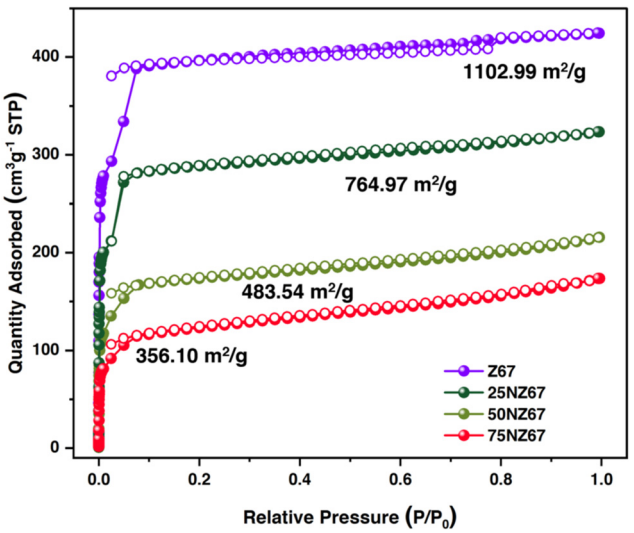

Fig. 2 N_2-adsorption desorption isotherms of **Z67** and **25/50/75NZ67**.

materials was also observed as the **NiV_{10}** loading increased. Furthermore, the average pore diameter showed a gradual increment while moving from **Z67** to **75NZ67** (Table S1), which can be attributed to the formation of a more open **Z67** framework and also the destruction of the small windows due to POM encapsulation.[43]

The compositional analyses of **Z67** and the nanocomposites were elucidated using ICP-MS, and the results are presented in Table S2. In the composites, as the concentration of **NiV_{10}** increases, the amount of vanadium (*i.e.*, mmol of vanadium per gram composite) also increases, with values of 0.84, 1.58, and 1.94 for **25NZ67**, **50NZ67**, and **75NZ67**, respectively. However, the Ni/V ratios observed for the composites (0.008–0.017) were much lower than that in the pristine **NiV_{10}** (0.2). This suggests a substantial detachment of Ni units from the **NiV_{10}** framework during the composite formation process.

XPS analyses

XPS data were collected to delve deeper into the composition of the surface elements and the electronic state variation of all the compounds. The deconvoluted C 1s scans of **Z67** and all three composites (Fig. S2) revealed two prominent peaks at 284.8 and 286.5 eV, attributed to the C–C/C=C and C–N bonds of 2-methyl imidazole.[44] Additionally, for the composites, the deconvoluted N 1s core-level regions involved three components: N_1 (399.1 eV) associated with 2-methylimidazole N atoms coordinated to Co nodes; N_2 (400.6 eV) assigned to H-bonded/protonated nitrogen (N–H/NH_4^+); and N_3 (407.1 eV) assigned to nitrates (NO_3^-).[45,46] Interestingly, the area of the N_1 component showed a gradual decrease in the three composites compared to **Z67** (Fig. S3). These observations strongly indicate that the interaction between V_{10} and **Z67** disrupts Co–N bonds, supporting the induction of defects in **Z67** in the form of undercoordinated Co nodes.[18] In the deconvoluted O 1s scans of **Z67** and composites (Fig. S4), O_1 (532.5 eV) is attributed to C–O from adventitious carbon, while O_2 (531.4 eV) is ascribed to the nitrates (NO_3^-).[47] Additionally, a consistent new peak is observed at ~290.50 eV for all three composites due to the lattice oxygens in the V_{10} clusters.[48] The appearance of this very peak indicates that the V_{10} species is widely distributed in the composites.[49] The deconvoluted Co 2p scans of the materials are shown in Fig. 3a. In the case of **Z67**, the peaks at 798.56 and 783.24 eV were attributed to Co^{2+}, and the peaks at 796.55 and 780.80 eV, along with the satellite peaks on the high binding energy side, were suggestive of Co^{3+}.[50] In the cases of the three composites, Co 2p spectra exhibited two pairs of spin–orbit doublets around ~798.64/783.40 eV and ~796.50/781.02 eV, corresponding to Co^{2+} and Co^{3+}, respectively. Notably, peak fitting analysis of Co 2p unveiled a significant variation in the relative ratio of Co^{2+} and Co^{3+}. While the Co^{2+}/Co^{3+} ratio was nearly equivalent in **Z67**, it depicted a much larger presence of Co^{3+} compared to Co^{2+} in all three composites (Fig. S5(a)). This can be interpreted by the partial destruction of the Co–N coordination bond by the interaction between V_{10} and **Z67** in all composites.[18,50] The pronounced increase in the % of Co^{3+} species across all the composites indicated their better electrochemical performance (discussed later), as Co^{3+} species are recognized as catalytically active centres for electrocatalytic OER.[50] Upon comparison of the deconvoluted V 2p scans of **NiV_{10}** and the composites (Fig. 3b), it was observed that in all three composites, the V 2p peaks corresponding to V $2p_{3/2}$ and V $2p_{1/2}$ of V^{5+} exhibited a shift towards lower binding energy compared to pristine **NiV_{10}**, indicating electronic charge redistribution within the composites. This redistribution seems to involve charge transfer from the **Z67** framework to the low-lying V-centred LUMOs of the decavanadate clusters, resulting in the reduction of some V^{5+} centres to V^{4+}, as evidenced by the appearance of V^{4+} peaks in all three composites. Furthermore, the intensity of the V^{4+} peaks increased with increasing **NiV_{10}** loading from **25NZ67** to **75NZ67**, reflecting a higher concentration of decavanadate units. Additionally, the overall increase in V 2p peak intensity confirms the progressive rise in POM content across the composite series (Fig. S5(b)). This charge transfer also facilitates partial oxidation of Co^{2+} to Co^{3+} within the framework, as discussed above.[18,19] The deconvoluted Ni 2p scan, as shown in Fig. 3c, revealed a low signal-to-noise ratio, likely attributable to the low nickel concentration in the composites. Nevertheless, the characteristic peaks at 855.7 and 873.3 eV are ascribed to Ni^{2+} in all three composites.[51] Additional features at 858.1 and 876.25 eV, attributable to Ni^{3+}, were also detected; however, these peaks could not be clearly resolved due to a low signal-to-noise ratio. As discussed earlier, **NiV_{10}** is prone to dissociation into decavanadate clusters and hydrated Ni^{2+} species in aqueous solution. This can result in the replacement of a small fraction of Co^{2+} centres within the **Z67** framework with Ni^{2+}, while a minor fraction of Ni^{3+} remains either adsorbed or incorporated in a different chemical environment, leading to peak broadening and low-intensity Ni^{3+} signals. Notably, with increasing Ni content in **50NZ67** and **75NZ67**, the signal-to-noise ratio improved. Table S3 shows the atomic % of the various elements calculated from the XPS spectra.

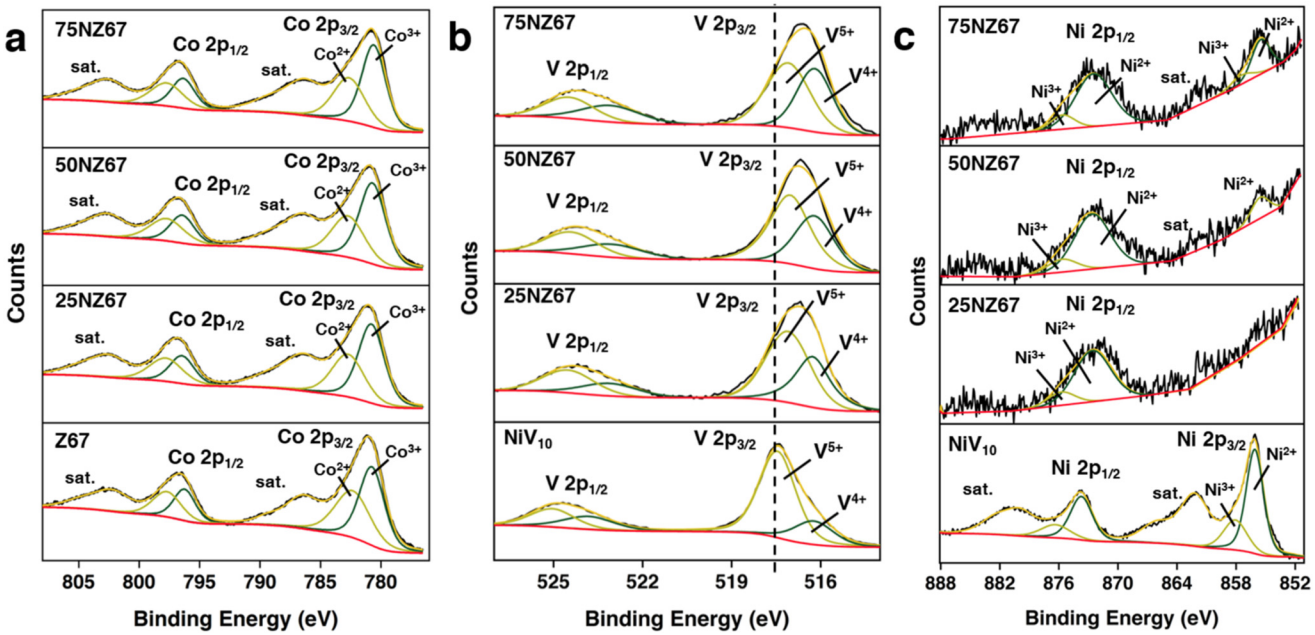

Fig. 3 (a) Deconvoluted Co 2p scans of **Z67**, **25NZ67**, **50NZ67**, and **75NZ67**; (b) deconvoluted V 2p scans of **NiV_{10}**, **25NZ67**, **50NZ67**, and **75NZ67** (black dashed line show the shift of the V^{5+} peak in V $2p_{3/2}$ region to lower binding energy sides in the composites with respect to **NiV_{10}**); and (c) deconvoluted Ni 2p scans of **NiV_{10}**, **25NZ67**, **50NZ67**, and **75NZ67**.

TGA was conducted on all samples to assess their thermal stability and validate their successful synthesis (Fig. S6). Notably, two distinct weight-loss regions were observed across all composites. The initial weight reduction observed up to 250 °C is attributed to the loss of solvated or coordinated water molecules in all composites. The pristine **Z67** exhibited weight loss in the 550 to 750 °C temperature range due to framework collapse. This phenomenon occurs at lower temperatures, *i.e.*, between 450 and 550 °C, for all the composites, which indicates the opening of the **Z67** framework in these composites due to interactions between V_{10} and **Z67**. Further, as the concentration of V_{10} increases in the composites, a corresponding decrease in the overall weight loss % was noted, resulting in a higher residual mass of **25/50/75NZ67** than **Z67**, as expected.

Microstructure analyses

FESEM images of all the samples were obtained to study the morphological differences in the composites and **Z67**. The FESEM images of **Z67** (Fig. 4a) showed representative dodecahedral-shaped particles possessing smooth surfaces with an average size of about ~550 nm (Fig. S7). In the case of **25NZ67**, there was a significant reduction in particle size to an average size of ~360 nm (Fig. S8); this decrease in particle size indicates that the loading of **NiV_{10}** has hindered the crystal growth in the composites, as reported earlier.[17,19] It was also observed that the particle morphology deviated slightly from that of the ideal **Z67**, with some broken edges and rougher surfaces of the dodecahedrons (Fig. 4b). The polyhedral geometry typical of **Z67** aggregates was still identifiable, along with minor structural disorders. Compared to **25NZ67**, a further increase in the concentration of V_{10} in the **50NZ67** and **75NZ67** composites led to a more open structure, as evident from Fig. 4c and d. The average size of the particles of **50NZ67** was calculated to

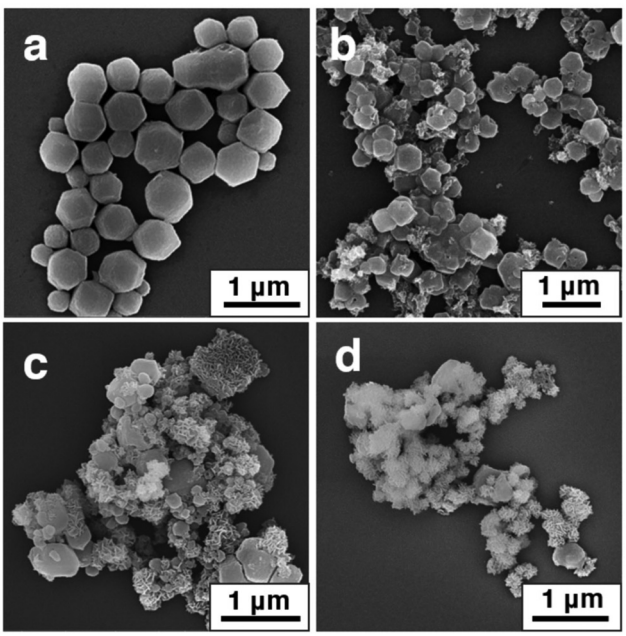

Fig. 4 FESEM images of (a) **Z67**; (b) **25NZ67**; (c) **50NZ67**; and (d) **75NZ67**, showing the change in the morphology from pristine **Z67**'s dodecahedral shaped polyhedra to small sized irregular polyhedra with rough surface and broken edges for the composites.

be ~370 nm (Fig. S9), while in the case of **75NZ67**, the **Z67** particles were not visible clearly. This is due to the distribution of the excess POMs on their surface, making it difficult to calculate their size from FESEM images. It can be noted that higher $\mathbf{NiV_{10}}$ loading in the composite leads to an excess of V_{10} clusters on the surface of the **Z67** particles. The morphological disorders and the framework opening observed in the polyhedral geometry of **Z67** due to composite formation contribute to the generation of undercoordinated Co nodes, leading to a decrease in crystallinity and microporosity, also evident from the XRD and BET data. These undercoordinated Co species are believed to play a pivotal role in enhancing the electrocatalytic activity of the materials.[19] SEM-EDS microanalysis (Fig. S10–S12) confirmed the presence of Co, V, Ni, and K in the composites. As the loading of $\mathbf{NiV_{10}}$ increases in the composites from **25NZ67** to **75NZ67**, the vanadium and nickel weight % also rises in the EDX data. However, the weight percentage of nickel is much lower than that of cobalt, confirming the presence of only a minute amount of nickel in the composites, as expected. Additional FESEM images can be found in Fig. S13.

Following this, TEM images of the materials were acquired to gain further insights into their structural features. The **Z67** particles displayed a characteristic hexagonal morphology with a smooth, finely textured surface (Fig. 5a). In comparison, the particles in all three composites (**25/50/75NZ67**) exhibited a notably rougher and more rugged surface texture than the original **Z67** particles, which can be attributed to incorporating V_{10} POM from $\mathbf{NiV_{10}}$. With increasing concentration of $\mathbf{NiV_{10}}$, some sheet-like aggregates were observed inside the **Z67** units and on their surface, fewer in **25NZ67** (Fig. 5b), more in **50NZ67** (Fig. 5c) and maximum in **75NZ67** (Fig. 5d). These are speculated to be the POMs, confirmed by the high-resolution TEM (HRTEM) images and elemental mapping at these positions, as discussed later. Images of individual particles from each composite (Fig. 5e-h) reveal the retained hexagonal morphology of **Z67**, along with rough edges and areas of dark contrast within the particles, further indicating the incorporation of POM units. The TEM analysis results of **50NZ67** and **75NZ67**, corroborated with their FESEM analysis, revealed an open structure of **Z67** particles with POM units distributed

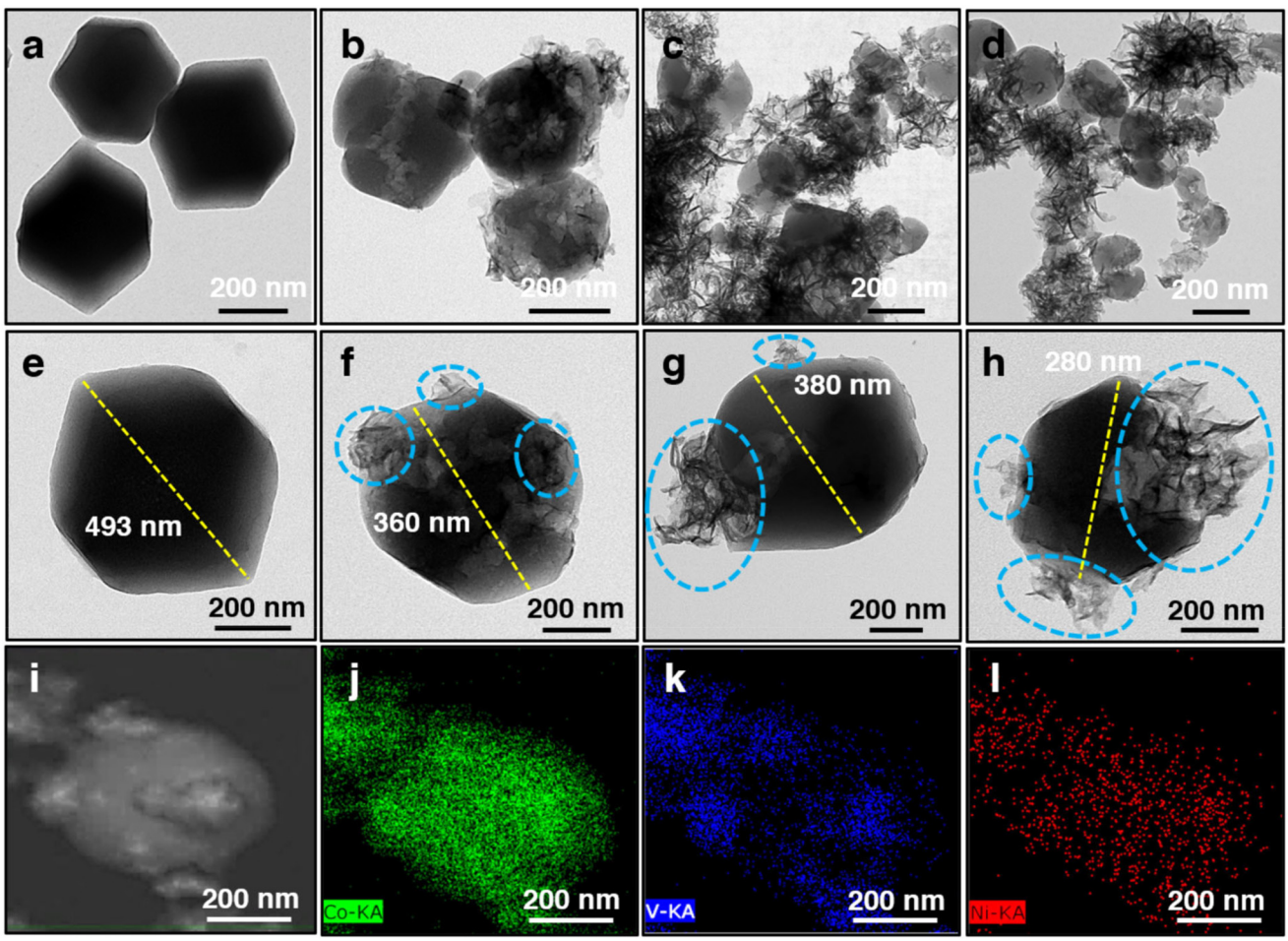

Fig. 5 TEM images of (a) **Z67**; (b) **25NZ67**; (c) **50NZ67**; and (d) **75NZ67**; (e-h) TEM images of a single particle of **Z67** and **25/50/75NZ67** (blue dotted regions showing the highly concentrated POM area on the surface of **Z67** particles); (i) elemental mapping area of **75NZ67**; elemental mapping showing the presence of (j) cobalt (green); (k) vanadium (blue); and (l) nickel (red).

both inside the pore and on the surface of the particles (Fig. 5g and h). Elemental mapping showed that the sheet-like aggregates inside and on the surface of **Z67** particles in these composites contained a significant % of V and O, suggesting that these are the POM units (Fig. 5i–l). As shown in Fig. S14–S19, elemental mapping clearly revealed the V, Ni, Co, K and O distribution in all these composites. Notably, the POM-enriched regions, identified as bright spots in the V mapping, are distinctly distinguishable from the nearly POM-free zones. Compared to V and O, the Ni patterns seem scattered in the whole region, similar to Co but in much less concentration, suggesting the presence of Ni along with Co in the whole **Z67** framework. The HRTEM images of the **25/50/75NZ67** revealed lattice fringes with a *d*-spacing of 0.24 nm, equal to that of the V_{10} POM (0.24 nm) (see Fig. S20). Additional TEM images of the materials are given in Fig. S21. Moreover, these fringes were exclusively found in the highlighted (blue circle) region of the composites. The observed *d*-spacings have also been confirmed by analyzing the selected area electron diffraction (SAED) patterns of the materials, as shown in Fig. S22. Based on all the structural and morphological analyses carried out, it can be concluded that all three composites show similar structural features. In all of them, some amounts of V_{10} clusters are encapsulated inside the **Z67** cavities, along with the distribution of excess POMs on the surface of the **Z67** particles, as revealed by the SEM and TEM data. This can also be seen from the BET data, which shows a decrease in surface area with increasing concentration of **NiV_{10}** in the composite. Apart from this, incorporating a few Ni centres in the **Z67** framework is anticipated from the ICP data, which shows the Ni/V ratio is much lower than it should be if the **NiV_{10}** structure were intact in the composites. More indication of the same can be seen in the XPS data, where a higher % of the mixed valent state of Co (resulting from the formation of CUMAS) and the presence of Ni can be observed as a result of V_{10} encapsulation and Ni incorporation. Further, the HRTEM analysis of the composites showed *d*-spacing values matching with the decavanadate POM, proving its distribution inside and outside the **Z67** framework. Alongside, the elemental mapping of the composites showed that the distribution of V was concentrated in the regions where the outgrowths were mainly observed, while the distribution of Ni appeared uniformly all over the framework. This again supports the fact that the Ni centres have uniformly replaced some Co centres in the **Z67** framework in the composites.

Electrochemical analyses

Electrochemical measurements were carried out using a standard three-electrode cell, having a working electrode tip with an electrocatalyst-modified glassy carbon (GC) rotating ring-disk electrode (RRDE) 4 mm in diameter, a reference electrode (Ag/AgCl, 4 M KCl (aq)), and platinum (Pt) wire as a counter electrode (CE). The applied potentials were measured against the Ag/AgCl reference electrode, and the measured $E_{Ag/AgCl}$ values were converted to the corresponding reversible hydrogen electrode (E_{RHE}) values using the Nernst equation conversion: $E_{RHE} = E_{Ag/AgCl} + 0.059\,pH + E^{\circ}_{Ag/AgCl}$ (with $E^{\circ}_{Ag/AgCl}$ = 0.197 V at 25 °C). The details related to the catalyst ink preparation and working electrode modification are given in the Experimental section. All the electrochemical tests were carried out in an N_2-saturated 0.1 M KOH electrolyte (pH = 13.0) prepared with deionized water. The electrocatalytic performances of the composites were evaluated through linear sweep voltammetry (LSV) polarization curves at a scan rate of 10 mV s^{-1} in 0.1 M KOH (pH = 13.0).

The redox behaviours of the materials in a 0.1 M KOH medium were analyzed using CV scans at a scan rate of 10 mV s^{-1} (Fig. S23). For all the materials under investigation, a characteristic distinct anodic peak around 1.12–1.18 V was observed, attributed to the Co^{2+} to Co^{3+} transition, while the corresponding reduction peak was observed around 1.02 V.[52,53] Compared to the characteristic Co^{2+}/Co^{3+} oxidation peak of **Z67**, all three composites exhibited a shift to lower potential, which could probably be related to electron transfer between **Z67** and decavanadate POM units, indicating a synergistic interaction between the two components as previously been shown in the XPS analysis. The encapsulation of the V_{10} clusters inside **Z67** cavities induced structural modifications to the **Z67** framework, resulting in the opening of **Z67** frameworks, leading to an increased number of Co centres undergoing redox processes. This also enhanced the electrochemical activity, as more intense and wider redox couples for the composites can be observed compared to those in pristine **Z67**.

For a better understanding of the synergistic interactions within the composites, we prepared a control sample, **Z67+NiV_{10}**, as a physical mixture of **Z67** and **NiV_{10}** through a simple room-temperature grinding method. The CV scans for **Z67**, **NiV_{10}**, **25NZ67** and **Z67+NiV_{10}** are presented in Fig. 6a. The Co^{2+}/Co^{3+} couple in **Z67** and **25NZ67** is denoted as A_1/C_1 and A_5/C_5, respectively, while the Ni^{2+}/Ni^{3+} couple in **NiV_{10}** is denoted as A_2/C_2. Notably, in **Z67+NiV_{10}**, two distinct redox couples A_3/C_3 and A_4/C_4 were observed. The A_3/C_3 couple corresponds to the A_2/C_2 couple seen for **NiV_{10}**, while the A_4/C_4 couple is analogous to the A_1/C_1 couple of **Z67**. This observation confirms that **Z67** and **NiV_{10}** exist as separate components in **Z67+NiV_{10}**. In contrast, **25NZ67** displays a single redox couple (A_5/C_5) shifted to a lower potential than the A_1/C_1 couple, a behaviour not present in the physical mixture. This indicates that the *in situ* prepared composites facilitate a reorganization of the **NiV_{10}** components, where some V_{10} clusters become encapsulated in the pores of **Z67**, and some Ni centres are incorporated into the **Z67** framework. Such unique arrangements are not achievable through simple physical mixing, highlighting that the synergistic effects of the components can only be realized when the composite is synthesized *in situ*. The less resolved Ni^{2+}/Ni^{3+} peak in the composites is not visible in the CV scans. This could be due to the large current density in the same potential region due to catalytic water oxidation, which masks the weaker Ni^{2+}/Ni^{3+}anodic peak. As anticipated, the Ni^{2+} to Ni^{3+} oxidative peaks in all three **25/50/75NZ67** composites are resolved in the DPV, as shown in Fig. S24.

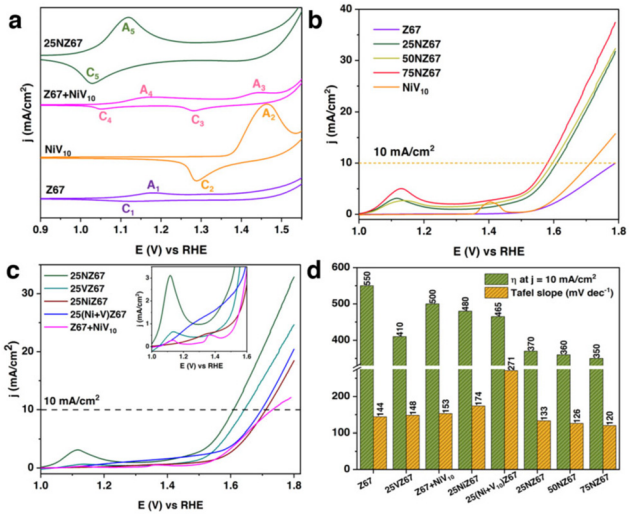

Fig. 6 (a) CV scans of **Z67**, **NiV_{10}**, **Z67+NiV_{10}** and **25NZ67** in 0.1 M KOH; (b) LSV scans of **Z67**, **NiV_{10}** and **25/50/75NZ67** in 0.1 M KOH; (c) LSV scans of **25NZ67**, and the control samples in 0.1 M KOH (inset: zoom-in view of the LSV scans in shorter potential window showing the most intense Co^{2+}/Co^{3+} oxidation peak for **25NZ67**, justifying its superior activity in comparison to the control samples.); and (d) comparison of OER parameters of **25/50/75NZ67** and the control samples.

Electrocatalytic OER

The electrocatalytic OER performance of the composites was assessed using LSV scans recorded at a scan rate of 10 mV s^{-1}. Fig. 6b shows that all three nanocomposites **25/50/75NZ67** showed higher current densities than **Z67** and **NiV_{10}**. This highlights the advantageous effect of the composite formation toward improving the OER electrocatalytic performance of the pristine **NiV_{10}** and **Z67** by utilizing the synergy of both components. The onset potential for all three composites was in the range of 1.44–1.46 V. The overpotential for **75NZ67** was 350 mV at j = 10 mA cm^{-2}, which was ~200 mV and ~130 mV lower than **Z67** and **NiV_{10}**, respectively, at the same current density. Additionally, **50NZ67** and **25NZ67** composites showed overpotentials of 360 mV and 370 mV, respectively. This trend can be attributed to the excess amounts of V_{10} and Ni in the composites with a higher loading of **NiV_{10}**, which results in a higher degree of structural defects in the **Z67** framework. This, in turn, generates a higher % of CUMAS, which facilitates faster OER kinetics and enhances charge transfer efficiency. The area under the anodic peak of the active species can be directly correlated to the amount of the active species responsible for OER present in the material.[54] Fig. S25 shows that **75NZ67** possesses the highest integrated area among the three composites, which explains its highest activity in the series.

We also prepared several control samples to assess the roles of the proposed Ni doping and *in situ* synthetic procedure in determining the OER activity of the composites **25/50/75NZ67**. First, we prepared a control sample, **25VZ67**, using only the sodium salt of decavanadate ($Na_6[V_{10}O_{28}]$) instead of **NiV_{10}** and keeping all other synthetic conditions unaltered. Therefore, in **25VZ67**, any possible Ni doping of **Z67** is prevented. Our second control sample was **Z67+NiV_{10}**, a physical mixture of **Z67** and **NiV_{10}**. This control compound was used to understand the potential role of the *in situ* synthetic conditions in composites **25/50/75NZ67**. Finally, to investigate the role of low-concentration nickel in the composites, we prepared two additional control samples by introducing nickel salt directly into the **Z67** and **25VZ67** systems, resulting in composites **25NiZ67** and **25(Ni+V)Z67**. Fig. 6c compares the LSV scans of **25NZ67** with the control samples, where the *in situ* prepared **25NZ67** composite showed a much better current density, lower onset, and a lower overpotential than all four control samples (**25VZ67**, **Z67+NiV_{10}**, **25NiZ67** and **25(Ni+V)Z67**). This observation confirms that better electrocatalytic activity of the *in situ* synthesized composites stems from the synergy of three components, *i.e.*, **Z67**, V_{10} and **Ni** centres. Such a synergy is not achievable by combining **Z67** with V_{10} alone, even under *in situ* conditions, or by physically mixing **Z67** and **NiV_{10}**, or by introducing Ni separately into **Z67** and **25VZ67** systems. The observed increment in the current density of the *in situ* generated composites **25/50/75NZ67** could be attributed to the generation of more undercoordinated Co and Ni centres in the modified **Z67** framework. Alongside this, the encapsulation of the V_{10} POMs in the **Z67** pores could be responsible for lowering the overpotential for OER. The characterization data for the control samples (FT-IR, XRD, and XPS) are given in Fig. S26–S33.

CV scans of **Z67** and **25/50/75NZ67** were recorded in a non-faradaic region at variable scan rates (100 mV s^{-1} to 600 mV s^{-1}) to calculate electrical double layer capacitance (C_{dl}), as shown in Fig. S34 and S35. The estimated C_{dl} values for the **25/50/75NZ67** composites were 0.29, 0.38, and 0.48 mF cm^{-2}, respectively. In contrast to **Z67**, which has a C_{dl} value of 0.14 mF cm^{-2}, all composites demonstrated higher C_{dl} values. The observed rise in the C_{dl} values of the composites suggests rougher areas on the electrode and more active sites within the composites.[55] The intrinsic activity of the electrocatalysts was evaluated by normalizing the average current densities from their LSV curves to their respective electrochemical surface area (ECSA). ECSA was calculated from the obtained C_{dl} values and considering a standard specific capacitance (C_s) value of 0.040 mF cm^{-2} according to similar reports[56] (Fig. S36). From this analysis, we observed that **25NZ67** exhibits the highest intrinsic activity among all composites, suggesting that the synergistic interactions between the three components (**Z67**, POM and Ni centres) in **25NZ67** enhance the activity of cobalt centres in the composite. For the higher loading composites (**50NZ67** and **75NZ67**), although they showed better intrinsic activity than pristine **Z67**, their intrinsic activity was lower than **25NZ67**. This indicates that in higher loading composites (**50**- and **75NZ67**), the enhanced overall current density arises predominantly from new active sites created by POM encapsulation and increased nickel content.

To get an insight into the kinetics of OER, the Tafel slopes (TS) of the materials were calculated from their LSV scans (Fig. S37). Among all the materials tested, **75NZ67** exhibited the lowest TS value of 120 mV dec^{-1}, compared to **50NZ67**

(126 mV dec^{-1}) and **25NZ67** (133 mV dec^{-1}). For OER electrocatalysis, a low TS value suggests faster reaction kinetics. As reported earlier, high TS values signify sluggish rate-determining steps involving the adsorption of OH^- on active sites, as in the case of **Z67** and other control samples. Consequently, the lower TS values suggest facile adsorption of OH^- groups onto the active sites, which is a direct consequence of the more open structures in the composites.[18] These results confirm that faster OER kinetics depends on the concentration of decavanadate POM and the Ni centres within the composites. Additionally, the faster kinetics observed for the composites **25/50/75NZ67**, compared to the control samples, underscores the importance of component synergy for achieving improved kinetics. A comparative plot of the overpotential @ j = 10 mA cm^{-2} and Tafel slope values of all the materials studied are given in Fig. 6d.

To investigate the electron transport capabilities of the composites **25/50/75NZ67**, electrochemical impedance spectroscopy (EIS) measurements were conducted at a steady potential of 1.55 V (Fig. 7). The impedance data were analysed using a Randles equivalent circuit, depicted in the inset of Fig. 7. In this model, R_s represents the solution resistance, while R_{ct} and C_{dl} correspond to the charge transfer resistance and the double-layer capacitance, respectively. The addition of a constant phase element (CPE) in the circuit arises from the non-ideal behaviour and complexity of the electrode/electrolyte interface.[57] In the Nyquist plot, the diameter of the semicircles corresponds to the charge transfer resistance (R_{ct}). Notably, the **25NZ67** composite exhibited a considerably lower R_{ct} of 50.05 Ω compared to the pristine **Z67**, which has an R_{ct} of 172.60 Ω. In the case of higher POM-loaded composites **50NZ67** and **75NZ67**, the R_{ct} values decreased further to 47.61 Ω and 44.06 Ω, respectively. These findings suggest that the encapsulation of POM within the ZIF cavity reduces the charge transfer resistance, leading to improved electrochemical performance during OER, as evidenced by the LSV curves. Other circuit fitting parameters are given in Table S4. Using the R_s value obtained from the EIS circuit fitting, the iR-corrected LSV plot was calculated (Fig. S38), which showed that **75NZ67** was the most active electrocatalyst for OER. A comparison plot of the η values at j = 10 and 20 mA cm^{-2} is given in Fig. S39.

Chronoamperometry was employed to evaluate the stability of the composites as OER electrocatalysts. The oxygen bubbles formed on the electrode surface are the source of the distinctive local current density reductions seen in the chronoamperometric plots shown in Fig. S40. Rotation of the electrode causes the bubbles to release, regaining some or all of the prior current density values.[58,59] As shown in Fig. 8a–c, the **25NZ67** composite demonstrated an approximately 8% increase in current density after an 8-hour chronoamperometry test, while the **50NZ67** composite exhibited a negligible 1% decrease. In contrast, the **75NZ67** composite experienced a significant decrease of 23% in current density. Regarding overpotentials at j = 10 mA cm^{-2}, the **25NZ67** composite maintained the same overpotential, whereas the **50NZ67** composite

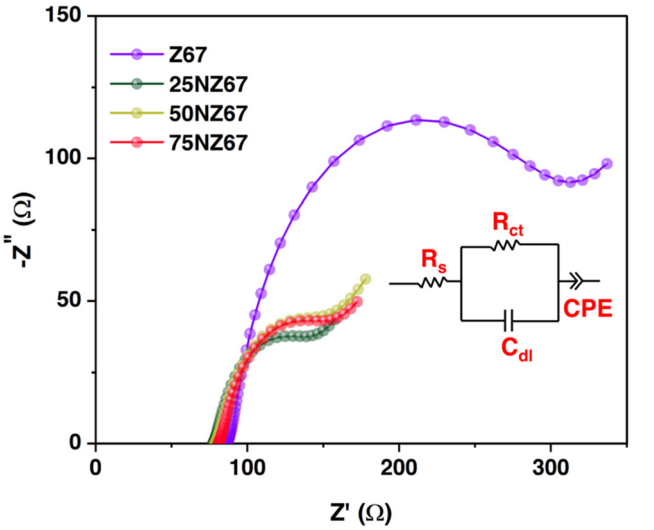

Fig. 7 EIS data of **Z67** and **25-75NZ67** measured at a steady potential of 1.55 V *vs.* RHE (inset: the fitted circuit model).

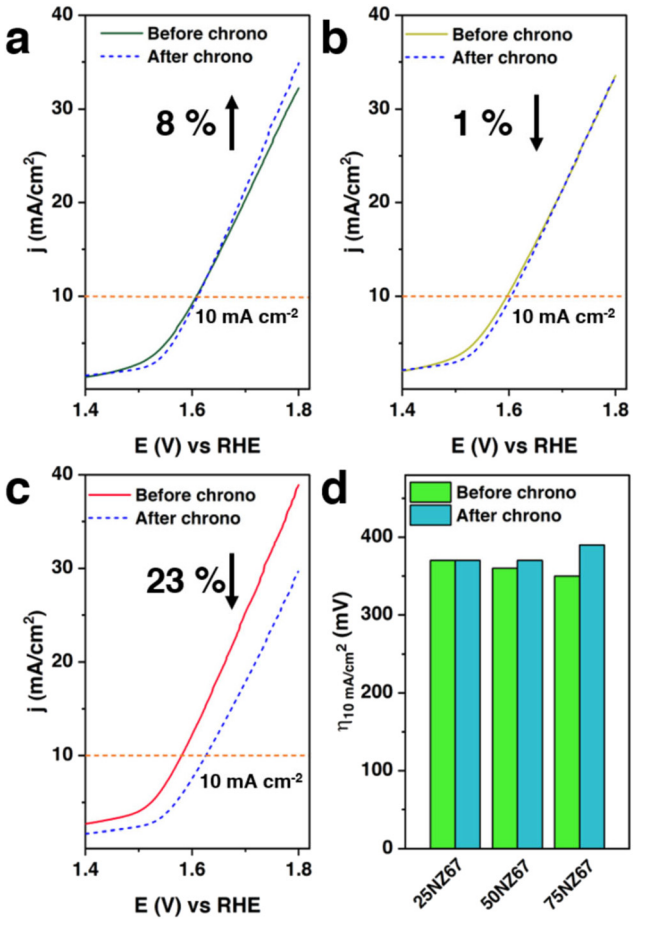

Fig. 8 LSV comparison of before and after 8 h chronoamperometry of (a) **25NZ67**; (b) **50NZ67**; and (c) **75NZ67**; (d) A comparative plot of the overpotentials @ j = 10 mA cm^{-2} before and after chronoamperometry.

showed an increase of 10 mV, and the **75NZ67** composite exhibited a 40 mV increase compared to the values before chronoamperometry (Fig. 8d). These variations in behaviour among the composites can be attributed to their distinct structural arrangements. The results indicate that the overall stability of the composites under OER conditions decreases as the POM content increases, highlighting the critical role of POM concentration for the long-term OER performance of these composites.

Due to the instability of POMs in the alkaline media, pristine **NiV_{10}** showed a decrease in current density (~8%), an increase in overpotential, and thus a poor overall stability after 8 h chronoamperometry, as reported earlier.[34] With **25NZ67**, we successfully addressed the instability issue that was faced in the case of pristine **NiV_{10}**, as we didn't observe any decrease in current density or change in overpotential during the 8 h chronoamperometry. For the other two composites, **50NZ67** and **75NZ67**, we hypothesize that due to comparatively more open polyhedral geometry and excess POMs on the surfaces of the **Z67** framework, there is a high possibility of POM leaching from the surface, resulting in a decrease in current density and an increase in overpotential, as observed. To prove our hypothesis, we recorded the UV-vis spectra of the recovered electrolytes of **25/50/75NZ67** post-chronoamperometry (Fig. S41). The UV-Vis spectrum of **NiV_{10}** in a 0.1 M KOH solution was taken as a reference sample, which displayed two peaks around 220 nm and 265 nm, assigned to the charge-transfer transition of the type $\pi(O) \rightarrow d(V)$ of the decavanadate POM.[60,61] Notably, the recovered electrolytes of **50NZ67** and **75NZ67** after the 8 h chronoamperometry experiment also showed a broad peak around 220 nm, indicating the leaching of vanadium species from the surface, which likely caused the reduction in OER activity. However, such leaching was not observed with the **25NZ67** composite, suggesting it is sufficiently stable under the given conditions.

To assess the post-OER stability of **25NZ67**, we conducted extensive analyses using FT-IR, XRD, XPS, SEM and TEM on the recovered sample after chronoamperometry. FT-IR spectra of the fresh and recovered **25NZ67** (Fig. 9a) revealed a decrease in the peak intensity, probably due to the very low amount of the sample recovered and used for IR studies and also due to the presence of acetylene black in the ink used for sample preparation for chronoamperometry. Apart from the decreased peak intensity, nearly all the peaks of the recovered **25NZ67** matched with the fresh catalyst, suggesting the catalyst's unaltered structure. The XRD pattern of the recovered catalyst (Fig. 9b) exhibited similarities to that of the fresh catalyst, with a higher signal-to-noise ratio attributable to amorphous acetylene black and a small amount of sample. This observation indicates no significant structural changes in the composite. The XPS results also indicated a similar elemental composition of the recovered and fresh catalysts. Furthermore, the deconvoluted Co 2p scan of the recovered **25NZ67** composite clearly depicted characteristic peaks of Co^{2+} (798.56 and 783.24 eV) and Co^{3+} (796.55 and 780.80 eV), along with their satellite peaks (Fig. S42). Despite some noise in the deconvoluted V 2p scan due to the limited sample recovery, the characteristic peak of V^{5+} remained discernible (Fig. S43). The FESEM images of the recovered catalyst (Fig. S44) showed mostly the morphology of acetylene black as spherical particles; however, some **Z67** polyhedra were still identifiable. The TEM and HRTEM images of the recovered catalyst showed a much clearer presence of the **Z67** particles and revealed a *d*-spacing of 0.24 nm, as seen for the fresh catalyst (Fig. 9c and d). These post-catalytic experiments demonstrate that the **25NZ67** composite retains its structural integrity and activity under OER conditions.

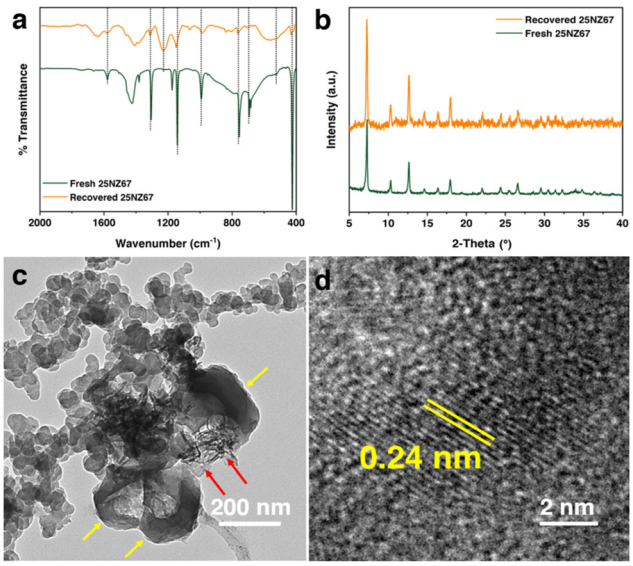

Fig. 9 (a) Comparison of FT-IR spectra of fresh and recovered **25NZ67** after 8 h chronoamperometry; (b) comparison of XRD spectra of fresh and recovered **25NZ67** after 8 h chronoamperometry; (c) TEM image of recovered **25NZ67** (yellow arrows show the **Z67** polyhedral architecture and red arrow show the presence of V_{10}); and (d) HRTEM image of the recovered **25NZ67** with *d*-spacing of 0.24 nm which matches with decavanadate.

Although a full explanation of the underlying mechanism is unclear, our initial studies provide some insights into the characteristics of active sites in the OER process. Wu *et al.* reported that there are four sequential electron-transfer phases in the OER mechanism in alkaline media, as follows:

$$OH^- + * \rightarrow OH* + e^-$$

$$OH* + OH^- \rightarrow O* + H_2O + e^-$$

$$O* + OH^- \rightarrow OOH* + e^-$$

$$OOH* + OH^- \rightarrow O_2 + H_2O + e^-$$

According to their report, for **Z67**, the rate-determining step (RDS) is the formation of OOH* from O*, which has a high energy barrier. They also documented, by DFT calculations, that upon the incorporation of a second transition metal ion into the **Z67** framework (Zn, Ni or Cu), the adsorption of O*, OH*, and OOH* is strengthened altogether, which facilitates the decrement of energy barrier for the RDS. This aids in

better electrocatalytic OER activity for the modified **Z67**.[62] Fernandez and co-workers have reported a bidirectional synergy upon encapsulating a Keggin POM inside **Z67**. The encapsulation resulted in the generation of CUMAS, which served as active centres for electrocatalytic OER.[19] In the same line of discussion, Co and a low concentration of Ni were identified as active metals in the present case. This was evidenced by the enhanced OER activity observed for all synthesized composites containing Ni compared to **Z67**, which lacks Ni. Also, the composites **25/50/75NZ67** showed better OER activity in terms of overpotential, current density and TS values than **25VZ67**, a control compound prepared by replacing **NiV_{10}** with simple V_{10} clusters during synthesis. A physical mixture of these components (**Z67+NiV_{10}**) further demonstrated that the mere presence of **NiV_{10}** is not enough for enhanced activity, which is achieved by the *in situ* synthesis. Thus, in **25NZ67**, the incorporation of a second metal center (Ni) in the **Z67** framework increases the overall active sites for electrocatalytic OER, which is evident from the integrated area of the LSV scans (Fig. S25). Also, the presence of Ni could make the adsorption of OH^- more feasible onto the catalyst surface, thus making the reaction easier. The second component of our composite, V_{10} clusters, on the other hand, plays the crucial role of modulating the local coordination environments in **Z67** framework, thus generating CUMAS, which helps in shifting the oxidation potential of the Co^{2+} centres to lower values, and also decreasing the overpotential for OER by facilitating a better charge transfer in the composites. Thus, the overall activity observed for the **25NZ67** is proposed to be a cumulative effect of the two strategies: (i) incorporation of a second transition metal in the **Z67** framework and (ii) encapsulation of POMs inside the **Z67** pores that were used for modification of **Z67**. Further, incorporating V_{10} clusters in the composite helps to reduce its charge transfer resistance, as revealed by the R_{CT} values calculated from the impedance measurements, contributing to the enhanced electrocatalytic OER activity of the composite.

A comparison of the current results with the OER parameters of similar ZIF and POM-based catalysts is given in Table S5. In a large number of strategies employed to enhance **Z67**'s OER activity,[63] researchers rely on high-temperature annealing, which destroys its inherent porous framework.[15,64] Other common approaches employed for activating ZIFs include metal ion doping,[13,65] POM hybridization,[66–68] carbonization, and forming composites with conductive supports.[69] While metal doping improves intrinsic activity by tuning the electronic structure, it risks distorting the ZIF framework. Simple POM hybridization introduces additional redox-active sites but often suffers from leaching issues. Carbonization enhances conductivity but sacrifices porosity and structural integrity, while conductive composites improve electron transport but usually require complex multi-step synthesis. In contrast, our approach uses **NiV_{10}** as a single precursor to simultaneously incorporate both nickel centres and decavanadate POM units at room temperature, without using any harsh reaction conditions. This strategy maintains the original **Z67** structure with only minor modifications (especially at lower loading of **NiV_{10}**), avoids harsh processing, and achieves strong synergistic electronic and redox interactions with low Ni content, offering a simpler and more effective route to enhance the electrocatalytic OER performance.

Conclusions

Herein, we have reported an approach by which a metal–organic framework is modified by incorporating a second transition metal (Ni) and a POM cluster (V_{10} clusters) into the framework structure for enhancing the electrocatalytic performance. This was achieved through an *in situ* synthesis of the MOF (**Z67**) in the presence of the labile all-inorganic coordination polymer $\{(H_2O)_2K\text{-}\mu\text{-}(H_2O)_3Ni(H_2O)_3\}_{2n}[V_{10}O_{28}]_n$ (**NiV_{10}**). The Ni centres, due to their labile coordination environment, partially dissociate in solution and are incorporated into the **Z67** framework alongside Co centres. Simultaneously, the appropriately sized V_{10} clusters are integrated both within the pores and on the external surface of **Z67**. The introduction of POMs units inside and outside the MOF cavities helps to enhance the number of coordinatively unsaturated metal active sites (CUMAS) and decrease the charge transfer resistance of the catalytic material. Control studies demonstrated a synergistic effect between the components of the composites, which can only be achieved by the *in situ* synthesis and not by physically mixing the components. The composites exhibited commendable performance for electrocatalytic OER with an overpotential of 350–370 mV at j = 10 mA cm^{-2} and TS values at 120–133 mV dec^{-1}. The composite with the highest **NiV_{10}** loading (**75NZ67**) showed the best OER activity, while it suffered from a decrement in stability under prolonged OER experiments due to excess POMs on the surface. On the other hand, the composite with the lowest **NiV_{10}** loading showed improved OER activity and the best stability among the three, confirming that an optimum loading of **NiV_{10}** is essential for obtaining high performance and stability for electrocatalytic OER. Overall, this work presents a promising route for the rational design of high-performance, noble-metal-free OER catalysts through the integration of labile POM-based coordination polymers within MOF architectures. These findings offer valuable insights for the future development of advanced electrocatalytic materials.

Experimental section

Materials and methods

$Co(NO_3)_2{\cdot}6H_2O$, $Ni(NO_3)_2{\cdot}6H_2O$ and acetylene black were purchased from Alfa Aesar, $NaVO_3$ was purchased from Loba Chemie, KOH and Nafion were purchased from Sigma Aldrich. All the solvents used were of spectroscopic grade. All the chemicals and reagents were used without further purification. **NiV_{10}** was synthesized as reported earlier.[33]

Physical characterization

FT-IR spectra were recorded on a Agilent Technology's Cary 600 Series instrument. The X-Ray Photoelectron Spectroscopy (XPS) of the hybrids was recorded on a Thermo Scientific NEXSA photo-emission spectrometer using Al-Kα (1486.6 eV) X-ray radiation. The raw data obtained from the instrument were processed using Avantage software. Inductively coupled plasma mass spectrometry (ICP–MS) measurements were carried out using an Agilent 7850 LC-ICP-MS instrument after digesting the samples in concentrated nitric acid. Nitrogen physisorption isotherms were evaluated using the Autosorb-iQ-MP/XR model of a Quantachrome instrument. Thermogravimetric analyses (TGA) were performed by using PerkinElmer Pyris 1 instrument. The sample (2 mg) was heated under a nitrogen atmosphere from room temperature to 800 °C at a heating rate of 5 °C min^{-1} with a flow rate of 20 mL min^{-1} in all the TGA experiments. The X-ray powder diffraction data were recorded on a Rigaku SmartLab 9 kW rotating anode X-ray diffractometer in Bragg–Brentano configuration using a Cu-sealed tube (Cu-Kα X-rays of 0.1541 nm) operating at 45 kV and 100 mA. The measurements were taken in the 2θ range 3–50° with a scan rate of 2° min^{-1} and a step size of 0.02°. The samples' morphological characterizations and energy-dispersive X-ray (EDX) spectral measurements were performed using Field Emission Scanning Electron Microscopy (FESEM, FEI Nova Nano SEM-450) and High-Resolution Transmission Electron Microscopy (HRTEM) using a FEI Tecnai G2 20 S-twin microscope operating at 200 kV. The average size of the particles was calculated using ImageJ software and FESEM and TEM images. The inter-fringe spacings were calculated using Gatan Microscope Suite 3 software.

Preparation of Z67

To a 25 mL methanolic solution of cobalt nitrate hexahydrate (0.722 g, 2.48 mmol), 25 mL methanolic solution of 2-methylimidazole (1.629 g, 19.84 mmol) was added. After 2.5 h of stirring, the resulting solid was collected by centrifugation and washed with water and methanol. The obtained powder was dried at 75 °C for 24 h.

Preparation of NiV_{10}-ZIF composites 25/50/75NZ67

To a 25 mL methanolic solution of cobalt nitrate hexahydrate (0.722 g, 2.48 mmol), 10 mL of aqueous **NiV_{10}** (0.025 g) solution was added and stirred at room temperature for 1 h. A 25 mL methanolic solution of 2-methylimidazole (1.629 g, 19.84 mmol) was then added to this solution and stirred for 2.5 h. After 2.5 h, the resulting solid was collected by centrifugation and washed successively with water and methanol. The powder thus obtained was dried at 75 °C for 24 h to get the composite **25NZ67**.

The same synthetic protocol was employed to synthesize the **50NZ67** and **75NZ67** composites as well, using 0.050 and 0.075 g of **NiV_{10}**, respectively.

During the synthesis of the composites **25/50/75NZ67**, the amounts of Co^{2+} salt and 2-MeIm (used for obtaining **Z67**) were kept constant in all the cases; only the **NiV_{10}** amount was varied to increase the loading amount sequentially. In that sense, the increasing amounts of **NiV_{10}** incorporated in these composites are with respect to the weight of the **Z67** counterpart.

Preparation of 25VZ67 composite

To a 25 mL methanolic solution of cobalt nitrate hexahydrate (0.722 g, 2.48 mmol), 10 mL of aqueous sodium salt of $Na_6[V_{10}O_{28}](H_2O)_n$ (0.025 g) was added and stirred at room temperature for 1 h. A 25 mL methanolic solution of 2-methylimidazole (1.629 g, 19.84 mmol) was then added to this solution and stirred for 2.5 h. After 2.5 h, the resulting solid was collected by centrifugation and washed successively with water and methanol. The powder thus obtained was dried at 75 °C for 24 h to get **25VZ67**.

Preparation of Z67+NiV_{10} physical mixture

As-synthesized **Z67** (0.085 g) was taken in a mortar along with 0.025 mg of **NiV_{10}**. These materials were ground together thoroughly for 1 h. The obtained fine powder was taken for the control studies.

Preparation of 25NiZ67

To a 25 mL methanolic solution of cobalt nitrate hexahydrate (0.722 g, 2.48 mmol), an aqueous solution (10 mL) of nickel nitrate hexahydrate (0.025 g, 0.086 mmol) was added and stirred at room temperature for 1 h. A 25 mL methanolic solution of 2-methylimidazole (1.629 g, 19.84 mmol) was then added to this solution and stirred for 2.5 h at room temperature. After 2.5 h, the resulting solid was collected by centrifugation and washed successively with water and methanol. The powder thus obtained was dried at 75 °C for 24 h to get **25NiZ67**.

Preparation of 25(Ni+V)Z67

To a 25 mL methanolic solution of cobalt nitrate hexahydrate (0.722 g, 2.48 mmol), 10 mL of aqueous sodium salt of $Na_6[V_{10}O_{28}](H_2O)_n$ (0.025 g) and nickel nitrate hexahydrate (0.025 g, 0.086 mmol) were added and stirred at room temperature for 1 h. A 25 mL methanolic solution of 2-methylimidazole (1.629 g, 19.84 mmol) was then added to this solution and stirred for 2.5 h at room temperature. After 2.5 h, the resulting solid was collected by centrifugation and washed successively with water and methanol. The powder thus obtained was dried at 75 °C for 24 h to get **25(Ni+V)Z67**.

Author contributions

R. K. S.: experimental data collection, data curation and analysis, manuscript writing (in parts); A. K.: ideation of overall work, data analysis, figure preparation, manuscript writing (in parts); A. H.: guidance in electrochemical analyses; C. P. P.: conceptualization, overall manuscript finalization.

Conflicts of interest

There are no conflicts to declare.

Data availability

The data supporting this article have been included as part of the SI. Additional characterization data for the materials: XRD, ICP-MS, TGA, FESEM, EDX, HRTEM, SAED, XPS; Electrochemical data: CV, LSV, DPV, ECSA, Tafel plot, chronoamperometry and postcatalytic characterization. See DOI: **https://doi.org/10.1039/d5dt01416f**.

Acknowledgements

CPP thanks SERB, DST, Govt. of India for financial support (project no. CRG/2023/003151) and AMRC, IIT Mandi for infrastructural facilities. A. K. and R. K. S. thanks MoE, Govt. of India for a Senior Research Fellowship, and AMRC for characterization facilities.

References

1 G. Gao, Z. Sun, X. Chen, G. Zhu, B. Sun, Y. Yamauchi and S. Liu, *Appl. Catal., B*, 2024, **343**, 123584.
2 C. C. L. McCrory, S. Jung, J. C. Peters and T. F. Jaramillo, *J. Am. Chem. Soc.*, 2013, **135**, 16977–16987.
3 Y. Lee, J. Suntivich, K. J. May, E. E. Perry and Y. Shao-Horn, *J. Phys. Chem. Lett.*, 2012, **3**, 399–404.
4 S. Piracha, Y. Zhang, A. Raza and G. Li, *Chem. Commun.*, 2024, **60**, 9918–9929.
5 U. Shahzad, M. Saeed, H. M. Marwani, J. Y. Al-Humaidi, S. u. Rehman, R. H. Althomali and M. M. Rahman, *Int. J. Hydrogen Energy*, 2024, **65**, 215–224.
6 A. Gaur, J. Sharma, D.-H. Lim, H. I. Lee and H. Han, *ChemCatChem*, 2025, **17**, e202401584.
7 V. R. Ramlal, K. B. Patel, S. K. Raj, D. N. Srivastava and A. K. Mandal, *ACS Appl. Mater. Interfaces*, 2024, **16**, 26034–26043.
8 N. Sun, S. S. A. Shah, Z. Lin, Y.-Z. Zheng, L. Jiao and H.-L. Jiang, *Chem. Rev.*, 2025, **125**, 2703–2792.
9 K. Li, T. Liu, J. Ying, A. Tian and X. Wang, *J. Mater. Chem. A*, 2024, **12**, 13576–13604.
10 P. Zhao, S. Fu, L. Cheng, Z. Jiao and M. Wu, *Coord. Chem. Rev.*, 2024, **498**, 215452.
11 Z. Li and S. Chaemchuen, *Chem. Rec.*, 2023, **23**, e202300142.
12 S. S. Sankar, G. Keerthana, K. Manjula, J. H. Sharad and S. Kundu, *Inorg. Chem.*, 2021, **60**, 4034–4046.
13 S. S. Selvasundarasekar, T. K. Bijoy, S. Kumaravel, A. Karmakar, R. Madhu, K. Bera, S. Nagappan, H. N. Dhandapani, G. A. M. Mersal, M. M. Ibrahim, D. Sarkar, S. M. Yusuf, S.-C. Lee and S. Kundu, *ACS Appl. Mater. Interfaces*, 2022, **14**, 46581–46594.
14 X. Guo, L. Li, S. Wang, H. Zhang, Y. Kuang, G. Duan and B. Cao, *Energy Adv.*, 2024, **3**, 654–663.
15 J. Wu, X. Sun, H. Chen, S. Guo, D. Hou, D. Wang and H. Wang, *Energy Fuels*, 2024, **38**, 7218–7230.
16 Y. Wang, Y. Wang, L. Zhang, C.-S. Liu and H. Pang, *Inorg. Chem. Front.*, 2019, **6**, 2514–2520.
17 Q. Y. Li, L. Zhang, Y. X. Xu, Q. Li, H. Xue and H. Pang, *ACS Sustainable Chem. Eng.*, 2019, **7**, 5027–5033.
18 V. K. Abdelkader-Fernández, D. M. Fernandes, S. S. Balula, L. Cunha-Silva and C. Freire, *J. Mater. Chem. A*, 2020, **8**, 13509–13521.
19 V. K. Abdelkader-Fernandez, D. M. Fernandes, S. S. Balula, L. Cunha-Silva and C. Freire, *ACS Appl. Energy Mater.*, 2020, **3**, 2925–2934.
20 S. Mukhopadhyay, J. Debgupta, C. Singh, A. Kar and S. K. Das, *Angew. Chem.*, 2018, **130**, 1936–1941.
21 A. Dymerska, B. Środa, K. Sielicki, G. Leniec, B. Zielińska, R. Zairov, R. Nazmutdinov and E. Mijowska, *J. Energy Chem.*, 2023, **86**, 263–276.
22 Y. Li, Z. Wang, J. Hu, S. Li, Y. Du, X. Han and P. Xu, *Adv. Funct. Mater.*, 2020, **30**, 1910498.
23 S. Liu, Y. Zhang, L. Hao, A. Nsabimana and S. Shen, *Sep. Purif. Technol.*, 2025, **354**, 129501.
24 M. T. Pope and A. Müller, *Angew. Chem., Int. Ed. Engl.*, 1991, **30**, 34–48.
25 L. Yang, J. Lei, J.-M. Fan, R.-M. Yuan, M.-S. Zheng, J.-J. Chen and Q.-F. Dong, *Adv. Mater.*, 2021, **33**, 2005019.
26 K. Dashtian, S. Shahsavarifar, M. Usman, Y. Joseph, M. R. Ganjali, Z. Yin and M. Rahimi-Nasrabadi, *Coord. Chem. Rev.*, 2024, **504**, 215644.
27 N. Li, J. Liu, B.-X. Dong and Y.-Q. Lan, *Angew. Chem., Int. Ed.*, 2020, **59**, 20779–20793.
28 Y. Zhang, Y. Li, H. Guo, Y. Guo and R. Song, *Mater. Chem. Front.*, 2024, **8**, 732–768.
29 T. Ma, R. Yan, X. Wu, M. Wang, B. Yin, S. Li, C. Cheng and A. Thomas, *Adv. Mater.*, 2024, **36**, 2310283.
30 V. K. Abdelkader-Fernández, D. M. Fernandes, S. S. Balula, L. Cunha-Silva and C. Freire, *ACS Appl. Energy Mater.*, 2020, **3**, 2925–2934.
31 H. Shi, H. Liang, F. Ming and Z. Wang, *Angew. Chem., Int. Ed.*, 2017, **56**, 573–577.
32 D. Jana, M. Alamgir and S. K. Das, *Inorg. Chem.*, 2024, **63**, 13959–13971.
33 D. Jana, H. K. Kolli, S. Sabnam and S. K. Das, *Chem. Commun.*, 2021, **57**, 9910–9913.
34 A. Kar, L. Sharma, A. Kumar, A. Halder and C. P. Pradeep, *Eur. J. Inorg. Chem.*, 2022, **2022**, e202101031.
35 R. Wei, X. Bu, W. Gao, R. A. B. Villaos, G. Macam, Z.-Q. Huang, C. Lan, F.-C. Chuang, Y. Qu and J. C. Ho, *ACS Appl. Mater. Interfaces*, 2019, **11**, 33012–33021.
36 K. C. Devarayapalli, S. V. P. Vattikuti, J. Lee, T. Kim and K. Lee, *Int. J. Energy Res.*, 2022, **46**, 12229–12240.
37 S. Wang, Y. Hou, S. Lin and X. Wang, *Nanoscale*, 2014, **6**, 9930–9934.
38 H. Wang, F.-X. Yin, B.-H. Chen, X.-B. He, P.-L. Lv, C.-Y. Ye and D.-J. Liu, *Appl. Catal., B*, 2017, **205**, 55–67.

39 A. Awadallah-F, F. Hillman, S. A. Al-Muhtaseb and H.-K. Jeong, *J. Mater. Sci.*, 2019, **54**, 5513–5527.
40 K. Zhou, B. Mousavi, Z. Luo, S. Phatanasri, S. Chaemchuen and F. Verpoort, *J. Mater. Chem. A*, 2017, **5**, 952–957.
41 X. Liu, W. Gong, J. Luo, C. Zou, Y. Yang and S. Yang, *Appl. Surf. Sci.*, 2016, **362**, 517–524.
42 A. F. Gross, E. Sherman and J. J. Vajo, *Dalton Trans.*, 2012, **41**, 5458–5460.
43 M. Jafarinasab and A. Akbari, *J. Environ. Chem. Eng.*, 2021, **9**, 106472.
44 A. Kale, R. Manikandan, C. J. Raj, A. D. Savariraj, C. Voz and B. Kim, *Mater. Today Energy*, 2021, **21**, 100736.
45 F. Tian, A. M. Cerro, A. M. Mosier, H. K. Wayment-Steele, R. S. Shine, A. Park, E. R. Webster, L. E. Johnson, M. S. Johal and L. Benz, *J. Phys. Chem. C*, 2014, **118**, 14449–14456.
46 L. Xiao, Q. Zhao, L. Jia, Q. Chen, J. Jiang and Q. Yu, *Electrochim. Acta*, 2019, **304**, 456–464.
47 S. Aduru, S. Contarini and J. W. Rabalais, *J. Phys. Chem.*, 1986, **90**, 1683–1688.
48 M.-Y. Zhang, Y. Song, X. Mu, D. Yang, Z. Qin, D. Guo, X. Sun and X.-X. Liu, *Small*, 2022, **18**, 2107689.
49 R. Zhu, J. Ding, Y. Xu, J. Yang, Q. Xu and H. Pang, *Small*, 2018, **14**, 1803576.
50 R. Zhu, J. Ding, J. Yang, H. Pang, Q. Xu, D. Zhang and P. Braunstein, *ACS Appl. Mater. Interfaces*, 2020, **12**, 25037–25041.
51 C. Zhang, X. Cai, Y. Qian, H. Jiang, L. Zhou, B. Li, L. Lai, Z. Shen and W. Huang, *Adv. Sci.*, 2018, **5**, 1700375.
52 S. Li, S. Peng, L. Huang, X. Cui, A. M. Al-Enizi and G. Zheng, *ACS Appl. Mater. Interfaces*, 2016, **8**, 20534–20539.
53 W. Zheng, M. Liu and L. Y. S. Lee, *ACS Catal.*, 2020, **10**, 81–92.
54 S. Anantharaj and S. Kundu, *ACS Energy Lett.*, 2019, **4**, 1260–1264.
55 N.-T. Suen, S.-F. Hung, Q. Quan, N. Zhang, Y.-J. Xu and H. M. Chen, *Chem. Soc. Rev.*, 2017, **46**, 337–365.
56 X. Li, S. You, J. Du, Y. Dai, H. Chen, Z. Cai, N. Ren and J. Zou, *J. Mater. Chem. A*, 2019, **7**, 25853–25864.
57 K. Panigrahi, S. Mal and S. Bhattacharyya, *J. Mater. Chem. A*, 2024, **12**, 14334–14353.
58 S. Hernández, G. Barbero, G. Saracco and A. L. Alexe-Ionescu, *J. Phys. Chem. C*, 2015, **119**, 9916–9925.
59 S. H. Ahn, I. Choi, H.-Y. Park, S. J. Hwang, S. J. Yoo, E. Cho, H.-J. Kim, D. Henkensmeier, S. W. Nam and S.-K. Kim, *Chem. Commun.*, 2013, **49**, 9323–9325.
60 B. Kortewille, O. Pfingsten, G. Bacher and J. Strunk, *ChemPhotoChem*, 2022, **6**, e202100120.
61 M. Louati, D. M. Neacsa, R. Ksiksi, C. Autret-Lambert and M. F. Zid, *J. Mol. Struct.*, 2022, **1250**, 131764.
62 J. Wu, Z. Yu, Y. Zhang, S. Niu, J. Zhao, S. Li and P. Xu, *Small*, 2021, **17**, 2105150.
63 H. Wen, S. Zhang, T. Yu, Z. Yi and R. Guo, *Nanoscale*, 2021, **13**, 12058–12087.
64 Y. Wu, Y. Wang, Z. Xiao, M. Li, Y. Ding and M.-l. Qi, *RSC Adv.*, 2021, **11**, 2693–2700.
65 S. Guo, J. Wu, H. Chen, D. Huan, H. Wang, D. Wang, D. Hou and X. Li, *ACS Appl. Energy Mater.*, 2025, **8**, 5770–5780.
66 Y. Tang, Z. Zou, X. Wu, P. Zuo, L. Wang, G. Huang, J. Zhu and S. Zhong, *New J. Chem.*, 2023, **47**, 9887–9893.
67 X. Zhao, Q. Zhang, X. Huang, L. Ding, W. Yang, C. Wang and Q. Pan, *Int. J. Hydrogen Energy*, 2022, **47**, 2178–2186.
68 D. Yin, M.-L. Wang, Y.-D. Cao, X. Yang, S.-Y. Ji, H.-P. Hao, G.-G. Gao, L.-L. Fan and H. Liu, *ACS Appl. Energy Mater.*, 2021, **4**, 6892–6902.
69 M. Cao, Y. Li, Y. Cao, Y. Wen, B. Li, Q. Shen and W. Gu, *Inorg. Chem.*, 2024, **63**, 14062–14073.

